



THIS MANUSCRIPT HAS BEEN SUBMITTED TO THE JOURNAL OF GLACIOLOGY AND HAS NOT BEEN PEER-REVIEWED.

Reconstructing subglacial lake activity with an altimetry-based inverse method

Journal:	<i>Journal of Glaciology</i>
Manuscript ID	JOG-23-0056.R1
Manuscript Type:	Article
Date Submitted by the Author:	n/a
Complete List of Authors:	Stubblefield, Aaron; Dartmouth College, Thayer School of Engineering Meyer, Colin; Dartmouth College, Thayer School of Engineering Siegfried, Matthew; Colorado School of Mines, Department of Geophysics Sauthoff, Wilson; Colorado School of Mines, Hydrologic Science and Engineering Spiegelman, Marc; Lamont-Doherty Earth Observatory, Earth and Environmental Science; Columbia University, Applied Physics and Applied Mathematics
Keywords:	Subglacial lakes, Antarctic glaciology, Subglacial processes, Ice-sheet modelling
Abstract:	Subglacial lake water-volume changes produce ice-elevation anomalies that provide clues about water flow beneath glaciers and ice sheets. Significant challenges remain in the quantitative interpretation of these elevation-change anomalies because the surface expression of subglacial lake activity depends on basal conditions, rate of water-volume change, and ice rheology. To address these challenges, we introduce an inverse method that reconstructs subglacial lake activity from altimetry data while accounting for the effects of viscous ice flow. We use a linearized approximation of a Stokes ice-flow model under the assumption that subglacial lake activity only induces small perturbations relative to a reference ice-flow state. We validate this assumption by accurately reconstructing lake activity from synthetic data that are produced with a fully nonlinear model. We then apply the method to estimate the water-

	<p>volume changes of several active subglacial lakes in Antarctica by inverting data from NASA's Ice, Cloud, and land Elevation Satellite 2 (ICESat-2) laser altimetry mission. The results show that there can be substantial discrepancies (20% or more) between the inversion and traditional estimation methods due to the effects of viscous ice flow. The inverse method will help refine estimates of subglacial water transport and further constrain the role of subglacial hydrology in ice-sheet evolution.</p>

SCHOLARONE™
Manuscripts

Reconstructing subglacial lake activity with an altimetry-based inverse method

Aaron G. STUBBLEFIELD,¹ Colin R. MEYER,¹ Matthew R. SIEGFRIED,^{2,3} Wilson SAUTHOFF,³ Marc SPIEGELMAN^{4,5}

¹*Thayer School of Engineering, Dartmouth College, Hanover, NH, USA*

²*Department of Geophysics, Colorado School of Mines, Golden, CO, USA*

³*Hydrologic Science and Engineering Program, Colorado School of Mines, Golden, CO, USA*

⁴*Lamont-Doherty Earth Observatory, Columbia University, Palisades, NY, USA*

⁵*Department of Applied Physics and Applied Mathematics, Columbia University, New York, NY, USA*

<aaron.g.stubblefield@dartmouth.edu>

ABSTRACT. Subglacial lake water-volume changes produce ice-elevation anomalies that provide clues about water flow beneath glaciers and ice sheets. Significant challenges remain in the quantitative interpretation of these elevation-change anomalies because the surface expression of subglacial lake activity depends on basal conditions, rate of water-volume change, and ice rheology. To address these challenges, we introduce an inverse method that reconstructs subglacial lake activity from altimetry data while accounting for the effects of viscous ice flow. We use a linearized approximation of a Stokes ice-flow model under the assumption that subglacial lake activity only induces small perturbations relative to a reference ice-flow state. We validate this assumption by accurately reconstructing lake activity from synthetic data that are produced with a fully nonlinear model. We then apply the method to estimate the water-volume changes of several active subglacial lakes in Antarctica by inverting data from NASA's Ice, Cloud, and land Elevation Satellite 2 (ICESat-2) laser altimetry mission. The results show that there can be substantial discrepancies (20% or more) between the inversion and traditional estimation methods due to the effects of viscous ice flow. The inverse method will help

28 **refine estimates of subglacial water transport and further constrain the role of**
29 **subglacial hydrology in ice-sheet evolution.**

30 INTRODUCTION

31 Ice-sheet surface elevation responds to a variety of time-varying subglacial phenomena, including subglacial-
32 lake volume change, basal-drag variations, and melting or freezing at the ice-water interface. Active sub-
33 glacial lakes (i.e., those that experience observable volume change in the observational record) in particular
34 have received much attention due to the localized perturbations they produce in ice-sheet surface elevation
35 during volume-change events (e.g., Gray and others, 2005; Wingham and others, 2006; Fricker and others,
36 2007). NASA's Ice, Cloud, and land Elevation Satellite (ICESat) mission (2003-2009) and the European
37 Space Agency's CryoSat-2 satellite altimetry mission (2010-present) facilitated the detection of over one
38 hundred active subglacial lakes beneath the Antarctic Ice Sheet (e.g., Smith and others, 2009; Wright and
39 Siegert, 2012; Fricker and others, 2016; Livingstone and others, 2022), driving investigations into their pos-
40 sible relation to fast ice flow (e.g., Stearns and others, 2008; Scambos and others, 2011; Siegfried and others,
41 2016) and into their ability to host microbial ecosystems (e.g., Christner and others, 2014; Achberger and
42 others, 2016; Davis and others, 2023). Fewer subglacial lakes have been discovered beneath the Greenland
43 Ice Sheet based on ice-surface changes, suggesting that there may be significant differences in subglacial
44 hydrological conditions there relative to the Antarctic Ice Sheet (e.g., Bowling and others, 2019; Livingstone
45 and others, 2019, 2022).

46 High-resolution satellite altimetry data from NASA's ICESat-2 mission (2018-present) presents a valu-
47 able opportunity to continue investigating dynamic conditions and constraining water budgets beneath ice
48 sheets (e.g., Markus and others, 2017; Neckel and others, 2021; Siegfried and Fricker, 2021). ICESat-2's
49 temporal resolution (91 day repeat cycle) and spatial resolution (~ 3.3 km across-track between beam pairs
50 and ~ 90 m between beams within the pairs) provide unprecedented coverage of active subglacial lakes,
51 which are typically greater than ~ 10 km in diameter and fill or drain over multiple years (Smith and others,
52 2009; Siegfried and Fricker, 2021; Stubblefield and others, 2021a). Modelling has shown that accurately
53 estimating subglacial-lake volume change, areal extent, and highstand or lowstand timing from altimetry
54 alone can be complicated by the effects of viscous ice flow (Stubblefield and others, 2021a). Basal verti-
55 cal velocity anomalies associated with subglacial lake activity can manifest with a wider areal extent and

56 smaller amplitude at the ice-sheet surface when ice flows laterally towards or away from the lake during
57 volume-change events. Ice viscosity, ice thickness, and basal drag exert strong control on ice flow and,
58 therefore, also influence the surface expression of subglacial lake activity (Stubblefield and others, 2021a).
59 Although satellite altimetry data has been incorporated in basal-drag inversions (e.g., Larour and others,
60 2014; Arthern and others, 2015; Goldberg and others, 2015; Mosbeux and others, 2016), inverse methods
61 that quantify subglacial-lake activity from altimetry and account for ice-flow effects have not yet been
62 developed.

63 Inversion of time-varying altimetry data necessitates leveraging reduced-order models to alleviate the
64 computational cost associated with repeatedly solving the forward problem. Dimensionality reduction
65 is often achieved using ice-flow models that are based on depth-integrated approximations of the Stokes
66 equations (e.g., Greve and Blatter, 2009). Solving the linearized Stokes equations on simplified domains
67 with spectral methods is an alternative way to achieve computational efficiency when the full stresses in the
68 ice must be resolved (e.g., Budd, 1970; Hutter and others, 1981; Balise and Raymond, 1985; Gudmundsson,
69 2003; Sergienko, 2012). Previous inversions relying on perturbation methods have not included time-varying
70 data (Gudmundsson and Raymond, 2008; Thorsteinsson and others, 2003). Likewise, a computational
71 method for inverting time-varying elevation data with perturbation-based models would be a valuable step
72 towards quantifying time-varying subglacial lake perturbations. We use this small-perturbation approach
73 as subglacial lake activity typically only induces small perturbations in ice-surface elevation (e.g., a few
74 meters) relative to ice thickness.

75 Here, we derive, test, and apply an altimetry-based inverse method for quantifying basal vertical ve-
76 locity perturbations that arise from subglacial lake activity. First, we outline the forward model for the
77 perturbation in ice-surface elevation that is produced by a basal vertical velocity forcing. We then derive the
78 inverse method from a least-squares optimization problem. To verify and validate the method, we present
79 tests with synthetic data from both the linearized and nonlinear models. We then apply the method to a
80 collection of active subglacial lakes in Antarctica (Figure 1). The results show that ice flow can produce
81 significant discrepancies between the inverse method and a traditional altimetry-based estimation method
82 for calculating changes in subglacial water volume over the current ICESat-2 time period. We conclude by
83 discussing limitations, extensions, and further applications of the method.

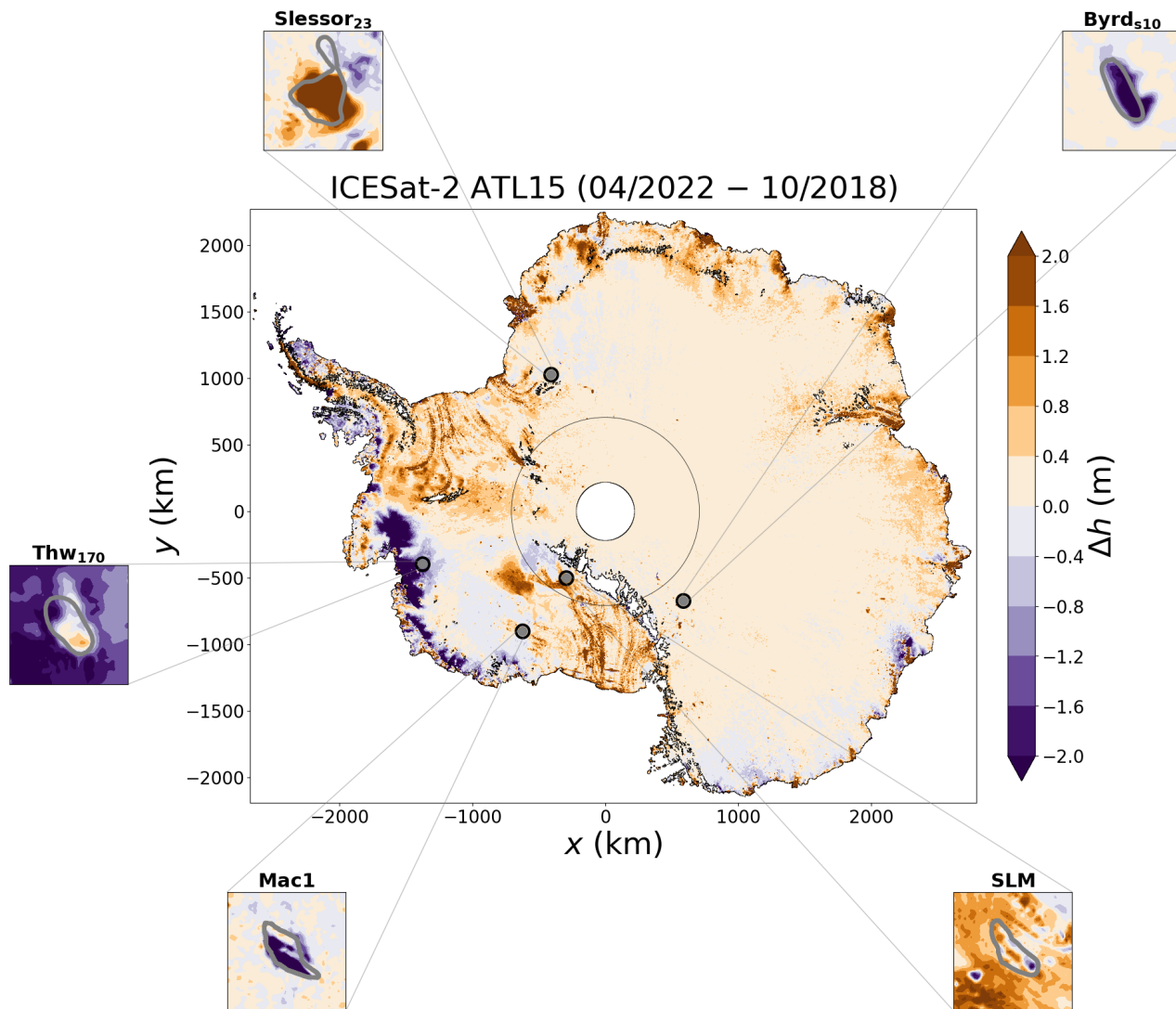


Fig. 1. Map of ICESat-2 ATL15 gridded product (Smith and others, 2022) showing the elevation change of the Antarctic Ice Sheet between October 2018 and April 2022. Insets show the locations of the subglacial lakes targeted as examples in this study. Subglacial lake boundaries derived from surface altimetry are shown as gray lines (Siegfried and Fricker, 2018). Regional thinning occurs around Thwaites Lake 170 (Thw₁₇₀) and regional thickening occurs around Mercer Subglacial Lake (SLM). Regional elevation-change trends around Slessor Glacier (lake Slessor₂₃), MacAyeal Ice Stream (lake Mac1), and Byrd Glacier (lake Byrd_{s10}) are less pronounced. We remove regional trends to produce elevation-change anomalies that are used in the inversions.

84 **METHOD**

85 In this section, we derive the forward model and the associated inverse method. First, we outline the
 86 general Stokes flow problem to highlight the governing equations and simplifying assumptions. Then, we
 87 outline a derivation of the small-perturbation model that is used in the inverse method. Finally, we derive
 88 the inverse method with a least-squares optimization approach.

89 **Stokes flow**

90 We assume that ice deforms as a viscous fluid according to the incompressible Stokes equations, which are
 91 given by

$$-\nabla \cdot \boldsymbol{\sigma} = \rho_i \mathbf{g} \quad (1)$$

$$\nabla \cdot \mathbf{u} = 0, \quad (2)$$

92 where ρ_i is the ice density, \mathbf{u} is the ice velocity, and $\mathbf{g} = g[0, 0, -1]^T$ denotes gravitational acceleration with
 93 magnitude $g = 9.81 \text{ m s}^{-2}$ (Greve and Blatter, 2009; Stubblefield and others, 2021b). We have excluded
 94 possible elastic components of ice deformation by assuming a viscous rheology and revisit this choice in
 95 the discussion. The stress tensor $\boldsymbol{\sigma}$ is defined via

$$\boldsymbol{\sigma} = -p\mathbf{l} + \eta \left(\nabla \mathbf{u} + \nabla \mathbf{u}^T \right) \quad (3)$$

96 where p is the pressure, \mathbf{l} is the identity tensor, and η is the viscosity. At the ice-bed boundary we assume
 97 a sliding law of the form

$$\mathbb{T}\boldsymbol{\sigma}\mathbf{n} = -\beta\mathbb{T}\mathbf{u} \quad (4)$$

98 where β is the basal drag coefficient, \mathbf{n} is an outward-pointing unit normal to the boundary, and $\mathbb{T} = \mathbf{l} - \mathbf{n}\mathbf{n}^T$
 99 is a projection tangential to the ice-sheet surface (Stubblefield and others, 2021b). Although the small-
 100 perturbation model used in the inversions assumes a Newtonian viscosity and linear sliding law (i.e.,
 101 constant η and β), we will also consider synthetic data produced by a fully nonlinear model with Glen's

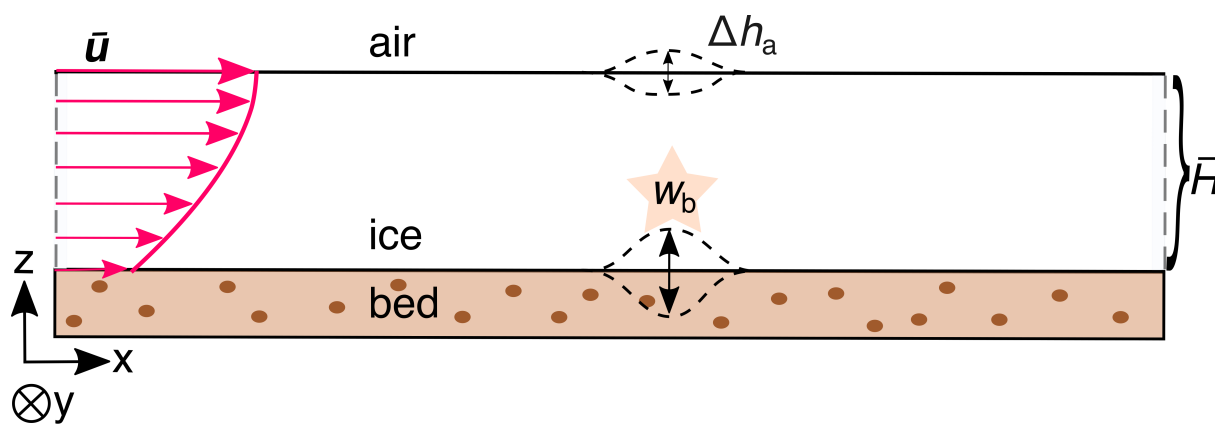


Fig. 2. Sketch of linearized model setup. The horizontal (map-plane) coordinates are (x, y) with the y direction pointing into the page. The basal vertical velocity anomaly w_b produces an elevation-change anomaly Δh_a . The ice thickness is \bar{H} and the horizontal surface velocity is \bar{u} in the reference flow state. The ice flow is aligned with the x axis here for simplicity but generally also has a component in the y direction. The volume change estimated from the elevation-change anomaly Δh_a can deviate significantly from the subglacial water-volume change (Stubblefield and others, 2021a).

102 law viscosity (Glen, 1955) and a nonlinear Weertman-style sliding law (Weertman, 1957) to test the validity
 103 of these simplifications.

104 The upper surface of the ice-sheet $z = h(x, y, t)$ evolves over time according to the kinematic equation

$$\frac{\partial h}{\partial t} + u \frac{\partial h}{\partial x} + v \frac{\partial h}{\partial y} = w \quad (5)$$

105 where the velocity components are evaluated at the surface ($z = h$). We assume that a stress-free condition

$$\boldsymbol{\sigma} \mathbf{n} = \mathbf{0} \quad (6)$$

106 holds at the upper surface of the ice sheet. We approximate the spatial domain as a horizontally unbounded
 107 slab because the ice-sheet extent is much greater than areal extent of the subglacial lakes. Away from the
 108 lake, we assume that all quantities approach an appropriate far-field reference state that is based on data
 109 and available ice-sheet model output.

110 Small-perturbation model

111 Now we will describe the forward model that is used in the inverse method. Although small-perturbation
 112 models have been derived previously, we outline a derivation here to highlight the assumptions underlying
 113 the inverse method (Balise and Raymond, 1985; Gudmundsson, 2003). Our goal is to find the basal vertical
 114 velocity perturbation w_b that produces the surface elevation-change anomaly Δh_a under the assumption
 115 that these anomalies arise from subglacial lake activity (Figure 2). We could also incorporate a basal drag
 116 anomaly to represent a slippery spot over a lake in the small-perturbation framework (e.g., Gudmundsson,
 117 2003; Stubblefield, 2022), but the resulting dipolar elevation-change anomaly (Sergienko and others, 2007)
 118 is not discernible in any of the active lakes considered herein. We revisit this idea in the discussion.

119 To derive a simplified model for this system, we assume that Δh_a and w_b are small perturbations from
 120 a known reference state that is (approximately) characterized by a constant ice thickness \bar{H} , horizontal
 121 surface velocity $\bar{\mathbf{u}} = [\bar{u}, \bar{v}]^T$, ice viscosity $\bar{\eta}$, and basal drag coefficient $\bar{\beta}$. We further assume that the basal
 122 surface is horizontal in the reference state and that the ice pressure equals the cryostatic pressure. Strictly
 123 speaking, an advective component is only present in the free-slip limit ($\bar{\beta} = 0$) under the assumption of
 124 a horizontally uniform Stokes flow over a flat bed subject to the stress boundary conditions (4) and (6).
 125 However, we retain a background advective velocity in all cases for consistency with the data.

126 Letting $[u_h, v_h, w_h]^T$ denote the perturbation in ice-sheet surface velocity, we insert perturbations to
 127 the reference states, $h = \bar{H} + \Delta h_a$ and $\mathbf{u} = [\bar{u}, \bar{v}, 0]^T + [u_h, v_h, w_h]^T$, into the kinematic equation (5) to
 128 obtain

$$\frac{\partial \Delta h_a}{\partial t} + \bar{u} \frac{\partial \Delta h_a}{\partial x} + \bar{v} \frac{\partial \Delta h_a}{\partial y} = w_h. \quad (7)$$

129 We have neglected terms involving products of perturbations in (7) under the assumption of small per-
 130 turbations. We solve equation (7) by taking Fourier transforms with respect to the horizontal coordinates
 131 (x, y) to obtain

$$\frac{\partial \widehat{\Delta h_a}}{\partial t} + (i\mathbf{k} \cdot \bar{\mathbf{u}}) \widehat{\Delta h_a} = \widehat{w_h}, \quad (8)$$

132 where $\mathbf{k} = [k_x, k_y]^T$ is the horizontal wavevector. The vertical surface velocity is assumed to satisfy the

133 Stokes flow problem (1)-(6), subject to the above simplifications, which allows us to derive a closed-form
 134 expression of the solution operator (Balise and Raymond, 1985; Gudmundsson, 2003; Stubblefield and
 135 others, 2021a).

136 We algebraically solve the Fourier-transformed Stokes problem to obtain an expression for the trans-
 137 formed vertical surface velocity,

$$\widehat{w}_h = -\mathcal{R}\widehat{\Delta h}_a + \mathcal{T}\widehat{w}_b, \quad (9)$$

138 in terms of the basal vertical velocity and surface elevation anomalies (e.g., Stubblefield and others, 2021a,
 139 Supporting Information). In equation (9), \mathcal{R} is a relaxation function that controls the decay rate of the
 140 elevation anomaly, and \mathcal{T} is a transfer function that maps the basal vertical velocity anomaly to its surface
 141 expression. These functions depend on the scaled wavevector magnitude $k' = |\mathbf{k}|\bar{H}$ and drag coefficient
 142 $\gamma = \bar{\beta}\bar{H}/(2\bar{\eta}k')$ through the relations

$$\mathcal{R} = \left(\frac{\rho_i g \bar{H}}{2\bar{\eta}k'} \right) \frac{(1 + \gamma)e^{4k'} - (2 + 4\gamma k')e^{2k'} + 1 - \gamma}{(1 + \gamma)e^{4k'} + (2\gamma + 4k' + 4\gamma k'^2)e^{2k'} - 1 + \gamma}, \quad (10)$$

143 and

$$\mathcal{T} = \frac{2(1 + \gamma)(k' + 1)e^{3k'} + 2(1 - \gamma)(k' - 1)e^{k'}}{(1 + \gamma)e^{4k'} + (2\gamma + 4k' + 4\gamma k'^2)e^{2k'} - 1 + \gamma}. \quad (11)$$

144 For a detailed derivation of the expressions (10) and (11) see, for example, Stubblefield and others (2021a,
 145 Supporting Information) and Stubblefield (2022, Appendix E).

146 Substituting the expression (9) into (8), we find that the ice-surface elevation anomaly Δh_a evolves in
 147 frequency space via

$$\frac{\partial \widehat{\Delta h}_a}{\partial t} + (i\mathbf{k} \cdot \bar{\mathbf{u}})\widehat{\Delta h}_a = -\mathcal{R}\widehat{\Delta h}_a + \mathcal{T}\widehat{w}_b. \quad (12)$$

148 The solution to equation (12) is given by

$$\widehat{\Delta h}_a = \widehat{\Delta h}_0 e^{-(i\mathbf{k} \cdot \bar{\mathbf{u}} + \mathcal{R})t} + \widehat{w}_b * \mathcal{K} \quad (13)$$

149 where $*$ denotes convolution over time and Δh_0 is the elevation perturbation at the initial time $t = 0$. The
 150 kernel \mathcal{K} , defined by

$$\mathcal{K} = \mathcal{T} e^{-(i\mathbf{k}\cdot\bar{\mathbf{u}}+\mathcal{R})t}, \quad (14)$$

151 controls the decay of the elevation-change anomaly and transfer of the basal anomaly to the surface. The
 152 characteristic time scale for the decay of surface-elevation anomalies is

$$t_{\text{relax}} = \frac{2\bar{\eta}}{\rho_i g \bar{H}}, \quad (15)$$

153 which controls the magnitude of the relaxation function \mathcal{R} (cf. Turcotte and Schubert, 2002, Chapter 6).
 154 The effects of viscous ice flow influence the surface expression of lake activity when the viscous relaxation
 155 time t_{relax} is comparable to the lake filling or draining timescale (Stubblefield and others, 2021a). We
 156 highlight the importance of the viscous relaxation time in the examples below.

157 Inverse method

158 Now we will outline the inverse method. We let \mathbf{F} denote the (map-plane) Fourier transform operator and
 159 define the relative elevation-change anomaly via

$$d = \Delta h_a - \mathbf{F}^{-1} \left(e^{-(i\mathbf{k}\cdot\bar{\mathbf{u}}+\mathcal{R})t} \mathbf{F}(\Delta h_0) \right), \quad (16)$$

160 which has the contribution from the initial value in equation (13) removed. From equation (13), we define
 161 the operator \mathbf{G} that maps w_b to the relative elevation change d via

$$\mathbf{G}(w_b) = \mathbf{F}^{-1}(\mathbf{F}(w_b) * \mathcal{K}) \quad (17)$$

162 where the kernel \mathcal{K} is defined in equation (14).

163 We consider a regularized least-squares objective functional,

$$J(w_b) = \frac{1}{2} \int_0^{t_f} \int_{-\infty}^{+\infty} \int_{-\infty}^{+\infty} |\mathbf{G}(w_b) - d|^2 dx dy dt + \frac{\varepsilon}{2} \int_0^{t_f} \int_{-\infty}^{+\infty} \int_{-\infty}^{+\infty} |\nabla w_b|^2 dx dy dt, \quad (18)$$

164 where t_f is the final time and the parameter ε controls the strength of the regularization term. While the

165 regularization in (18) promotes smoothness, other regularizations could be chosen to promote sparsity of
 166 the basal forcing, for example (Stadler, 2009). The minimizer of the objective (18) satisfies the normal
 167 equation

$$\mathbf{G}^*(\mathbf{G}(w_b)) - \varepsilon \nabla^2 w_b = \mathbf{G}^*(d), \quad (19)$$

168 which can be derived with variational calculus (Vogel, 2002; Hanke, 2017). The adjoint operator \mathbf{G}^* in (19)
 169 is given by

$$\mathbf{G}^*(f) = \mathbf{F}^{-1}(\mathbf{F}(f) \star \mathcal{K}) \quad (20)$$

170 for any function f , where \star denotes cross-correlation over time.

171 We solve the equation (19) with the conjugate gradient method to obtain the basal vertical velocity w_b .
 172 In using the conjugate gradient method to solve this operator equation, we avoid explicitly constructing
 173 matrices corresponding to the forward and adjoint operators, and instead simply require the action of
 174 these operators on functions (Atkinson and Han, 2009, Section 5.6). We implemented the discretized
 175 inverse method in Python with SciPy's fast Fourier transform and convolution algorithms (Virtanen and
 176 others, 2020). The code is openly available (<https://doi.org/10.5281/zenodo.8371416>).

177 Estimation of water-volume change

178 To compare the inversion with previous estimation methods, we will focus on estimating subglacial water-
 179 volume changes. Given the basal vertical velocity inversion w_b , the basal water-volume change over a
 180 map-plane area B can be computed via

$$\Delta V_{\text{inv}}(t) = \int_0^t \left[\iint_B w_b \, dx \, dy \right] dt'. \quad (21)$$

181 Alternatively, the volume-change has often been estimated in previous studies by integrating the elevation
 182 change anomaly over the static outline of a lake (Fricker and Scambos, 2009; Smith and others, 2009).
 183 Using this approach, the water-volume change is estimated by

$$\Delta V_{\text{alt}}(t) = \iint_B \Delta h_a - \Delta h_0 \, dx \, dy, \quad (22)$$

184 where we have integrated over the same map-plane area B . Although an alternative lake boundary could
185 be identified with the inversion, we use the same boundary to calculate both estimates for consistency in
186 comparison. We revisit this problem in the discussion.

187 In the limits $\mathcal{R} \rightarrow 0$ and $\mathcal{T} \rightarrow 1$, equation (12) implies that these volume changes are equivalent (i.e.,
188 $\Delta V_{\text{inv}} = \Delta V_{\text{alt}}$). This “rigid-ice” limit is approached when the ice is viscous enough for the relaxation
189 timescale, t_{relax} (eq. 15), to greatly exceed the volume-change timescale (Stubblefield and others, 2021a).
190 Although incompressibility causes these volume changes to be equal when integrating over the entire areal
191 extent of a glacier, this approach is impractical for the Antarctic Ice Sheet due to the presence of multiple
192 lakes and regional thickening or thinning trends. We explore the discrepancy between the inversion-derived
193 estimate (21) and surface-derived estimate (22) for a range of parameters in the examples below.

194 SYNTHETIC EXAMPLES

195 Before applying the method to the ICESat-2 altimetry data, we first solve two problems with synthetic data
196 to validate the method and illustrate the range of behaviours found in the ICESat-2 examples below. First,
197 we verify the implementation by inverting synthetic data that is produced by prescribing the linearized
198 model with a known basal vertical velocity field and then adding Gaussian white noise to the resulting
199 elevation change. For consistency with the ICESat-2 examples, we remove a small off-lake elevation-change
200 component, Δh_{off} , from the elevation change as detailed in the next section. For this example, we choose a
201 basal vertical velocity field that is a Gaussian bump undergoing sinusoidal oscillations in time. The inverse
202 method is able to reconstruct the basal vertical velocity and volume-change time series from the synthetic
203 data (Figure 3). We find that there is little deviation ($\lesssim 5\%$) between the volume-change estimates (21) and
204 (22) on short timescales (i.e., less than ~ 2.5 years), whereas large deviations occur over decadal timescales.
205 This behavior arises because the viscosity is $\bar{\eta} = 10^{15}$ Pa s for this example, leading to characteristic
206 relaxation timescale of $t_{\text{relax}} \approx 2.8$ yr. These results highlight that there will not be significant deviations
207 between the altimetry-based and inversion-based volume-change estimates over the current ICESat-2 time
208 period if the ice viscosity reaches this magnitude. We provide an example of this behavior below. In all
209 examples herein, we set the regularization parameter to $\varepsilon = 1$ in equation (19), which results in accurate
210 reconstructions of the synthetic examples without over-fitting the data.

211 Next, we show an example with synthetic data produced by a fully nonlinear model to test the assump-
212 tions underlying the small-perturbation approach (Stubblefield and others, 2021b,a). The nonlinear model

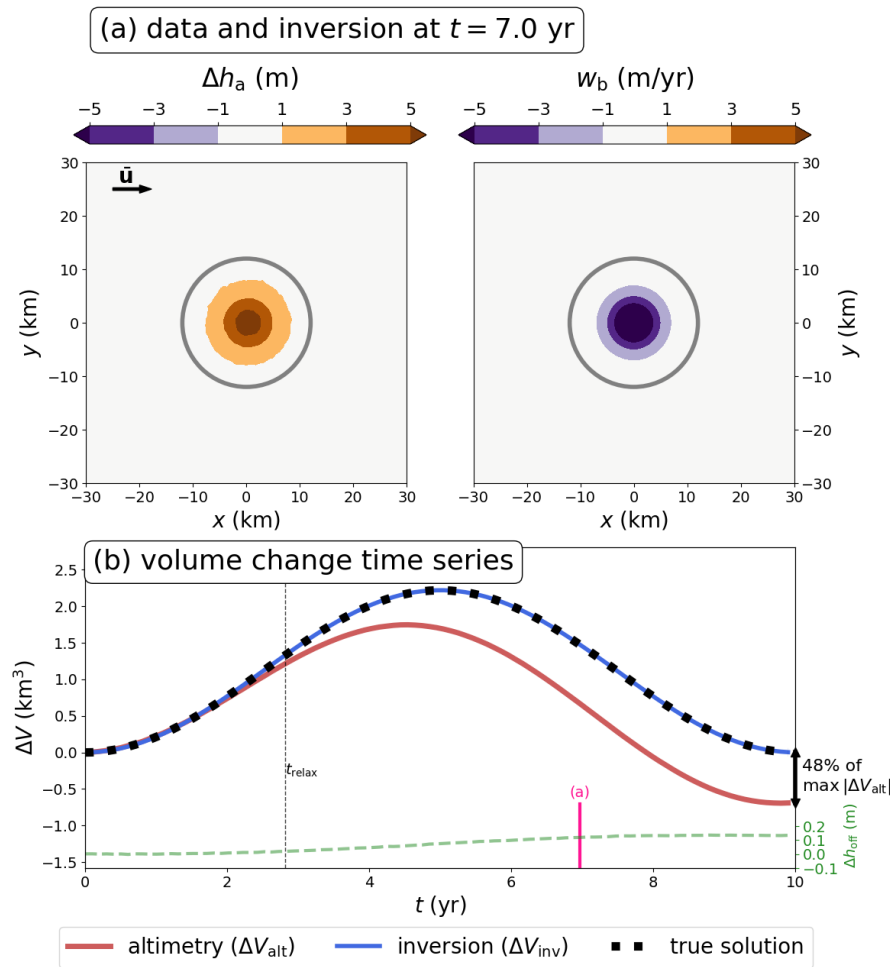


Fig. 3. Inversion results for synthetic data produced with the linearized model. (a) Map-plane elevation anomaly and inversion at $t = 7$ yr. (b) Time series of the surface-derived volume change (ΔV_{alt}), the inversion-based volume change (ΔV_{inv}), and the off-lake component (Δh_{off}) that is removed prior to inversion. The gray contours in (a) and (b) show the boundaries used to compute the volume-change time series. The ice flow direction is shown by the black arrow in (a). The maximum deviation between the surface-derived volume change and the inversion in (b) is 0.83 km^3 , or 48% of the maximum amplitude of the surface-derived estimate. The inversion accurately recovers the true water-volume change (dashed black line). The parameters for this example are $\bar{H} = 2500 \text{ m}$, $\bar{\eta} = 10^{15} \text{ Pa s}$, $\bar{\beta} = 10^{11} \text{ Pa s m}^{-1}$, $\bar{u} = 200 \text{ m yr}^{-1}$, and $\bar{v} = 0 \text{ m yr}^{-1}$. The viscous relaxation time associated with these parameters is $t_{\text{relax}} = 2.82 \text{ yr}$. The pink line marks the time step shown in (a). See Movie S1 for an animation of the inversion over all time steps.

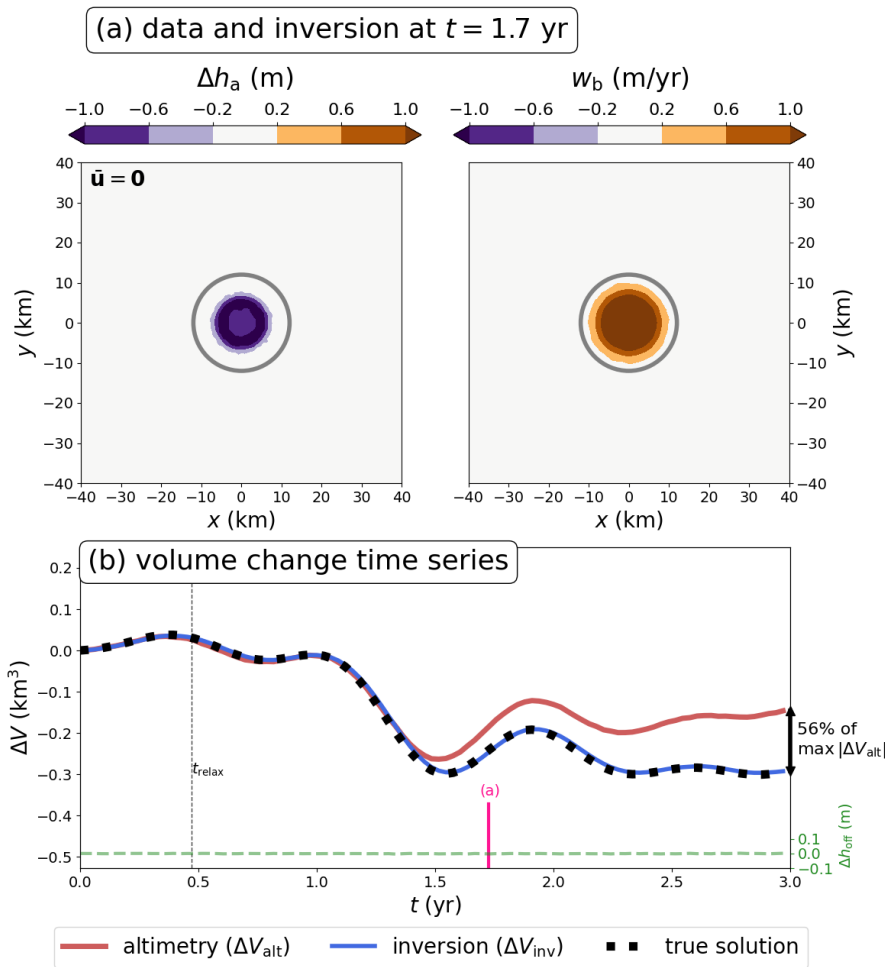


Fig. 4. Inversion results for synthetic data produced with a radially-symmetric nonlinear Stokes model (Stubblefield and others, 2021b). (a) Map-plane elevation anomaly and inversion at $t = 1.7$ yr. (b) Time series of the surface-derived volume change (ΔV_{alt}), the inversion-based volume change (ΔV_{inv}), and the off-lake component (Δh_{off}) that is removed prior to inversion. The gray contours in (a) and (b) show the boundaries used to compute the volume-change time series. The maximum deviation between the surface-derived volume change and inversion in (b) is 0.15 km^3 , or 56% of the maximum amplitude of the surface-derived estimate. The inversion accurately recovers the true water-volume change (dashed black line). The parameters for this example are $\bar{H} = 1500 \text{ m}$, $\bar{\eta} = 10^{14} \text{ Pa s}$, $\bar{\beta} = 10^{10} \text{ Pa s m}^{-1}$, $\bar{u} = 0 \text{ m yr}^{-1}$, and $\bar{v} = 0 \text{ m yr}^{-1}$. The viscous relaxation time associated with these parameters is $t_{\text{relax}} = 0.47 \text{ yr}$. The pink line marks the time step shown in (a). See Movie S2 for a detailed animation of the nonlinear model and Movie S3 for an animation of the inversion over all time steps.

213 assumes a Glen's law viscosity (Glen, 1955; Cuffey and Paterson, 2010), a nonlinear Weertman-style sliding
 214 law (Weertman, 1957), fully nonlinear surface kinematic equations, and vanishing basal drag over the lake.
 215 For this example, we have assumed radial symmetry with respect to the map-plane coordinates (x, y) to
 216 facilitate numerical solution in three spatial dimensions. We also prescribe a more complex volume-change
 217 time series with a duration of three years in accordance with the current ICESat-2 time span and choose
 218 a lower viscosity for this example, $\bar{\eta} = 10^{14}$ Pa s (Figure 4). Despite the simplifications inherent to the
 219 inverse method, the inversion accurately recovers the volume change time series that is produced by the
 220 nonlinear model (Figure 4). Most importantly, the inversion is much more accurate than the surface-based
 221 volume change for this parameter regime. This example shows that ice viscosities on the order of $\bar{\eta} = 10^{14}$
 222 Pa s can result in significant volume-change deviations over the current ICESat-2 time span. In particular,
 223 the examples in Figure 3 and Figure 4 show that the altimetry-based estimate tends to underestimate the
 224 magnitude of the true water volume change, regardless of whether the volume change is positive or negative.
 225 Next, we describe the data and preprocessing steps before discussing examples of ICESat-2 inversions.

226 DATA AND PREPROCESSING

227 We use the ICESat-2 ATL15 L3B Gridded Antarctic and Arctic Land Ice Height Change (Version 2) data
 228 product (Smith and others, 2022) to obtain elevation-change anomalies above the Antarctic subglacial
 229 lakes shown in Figure 1. For the examples explored here, we interpolated the ICESat-2 ATL15 data onto
 230 a space-time grid with 100 points in each direction (t, x, y) to obtain the same resolution as the numerical
 231 model. Alternatively, we could restrict the model-data misfit in (18) to the discrete set of data points, but
 232 this could require additional temporal regularisation that we have not included in this study. We remove
 233 any regional thickening or thinning trends by subtracting the spatially averaged off-lake component, Δh_{off} ,
 234 as described below. We also have to establish a reference elevation profile to define the elevation-change
 235 anomaly. By default, the elevation changes in ATL15 are relative to the ice-surface elevation on January
 236 1, 2020. In general, the elevation anomaly can be defined relative to any of the ATL15 time points by
 237 subtracting the elevation surface at a particular reference time t_{ref} . Therefore, the elevation change anomaly
 238 is derived from the ATL15 elevation change product Δh via

$$\Delta h_a(x, y, t) = \Delta h(x, y, t) - \Delta h_{\text{off}}(t) - [\Delta h(x, y, t_{\text{ref}}) - \Delta h_{\text{off}}(t_{\text{ref}})] \quad (23)$$

Table 1. Parameters used in the inversions of the Antarctic subglacial lakes shown in Figure 1. Data sources are described in the “Data and Preprocessing” section.

Parameter	units	Mac1	SLM	Slessor ₂₃	Thw ₁₇₀	Byrd _{s10}
\bar{H} : ice thickness	m	926	1003	1735	2558	2676
$\bar{\eta}$: ice viscosity	Pa s ($\times 10^{14}$)	2.3	2.2	2.4	5.7	50.0
$\bar{\beta}$: basal drag coefficient	Pa s m ⁻¹ ($\times 10^{10}$)	7.4	37.0	2.7	1.3	14.0
\bar{u} : surface velocity (x)	m yr ⁻¹	334	172	-141	-130	-9.4
\bar{v} : surface velocity (y)	m yr ⁻¹	-178	-65	-146	-78	-9.8

where Δh_{off} is the (time-varying) spatial average of Δh away from the lake. Here, the spatial average is taken over all points that are at a distance greater than 80% from the centroid of the lake to the boundary of the computational domain.

Based on previously identified lake activity, an appropriate reference time t_{ref} to define the anomalies happens to be the initial time in the ATLL15 product, October 1, 2018, for all of the lakes considered here except Mercer Subglacial Lake (SLM). SLM reached an apparent highstand near the end of 2017 before beginning a drainage event during the ICESat-2 period (Siegfried and Fricker, 2021), so the initial time in the ICESat-2 data does not correspond to an elevation anomaly of zero. We elaborate on this decision for each lake in more detail below and provide further commentary on preprocessing considerations in the discussion.

To invert the elevation-change data, we also must supply the approximate ice thickness \bar{H} , ice viscosity $\bar{\eta}$, basal drag coefficient $\bar{\beta}$, and horizontal ice velocity $\bar{\mathbf{u}} = [\bar{u}, \bar{v}]^T$ that describe the reference ice-flow state (Figure 2). The viscosity and basal drag estimates are derived from the inversions presented in Arthern and others (2015), which relied on the ALBMAP ice thickness (Le Brocq and others, 2010) and the MEaSURES InSAR-Based Antarctic Ice Velocity Map (Version 1) (Rignot and others, 2011; Mouginot and others, 2012). However, we obtain horizontal surface velocity from the MEaSURES Phase-Based Antarctic Ice Velocity Map (Version 1) (Mouginot and others, 2019a,b) and ice thickness from MEaSURES BedMachine Antarctica (Version 3) (Morlighem and others, 2020; Morlighem, 2022) for greater compatibility with the ICESat-2 epoch. All parameter values are obtained by calculating the mean of these data over the extent of the computational domain. The parameter values for each example are reported in Table 1 and the figure captions. To define the boundaries B in the volume estimation equations (21) and (22), we use the

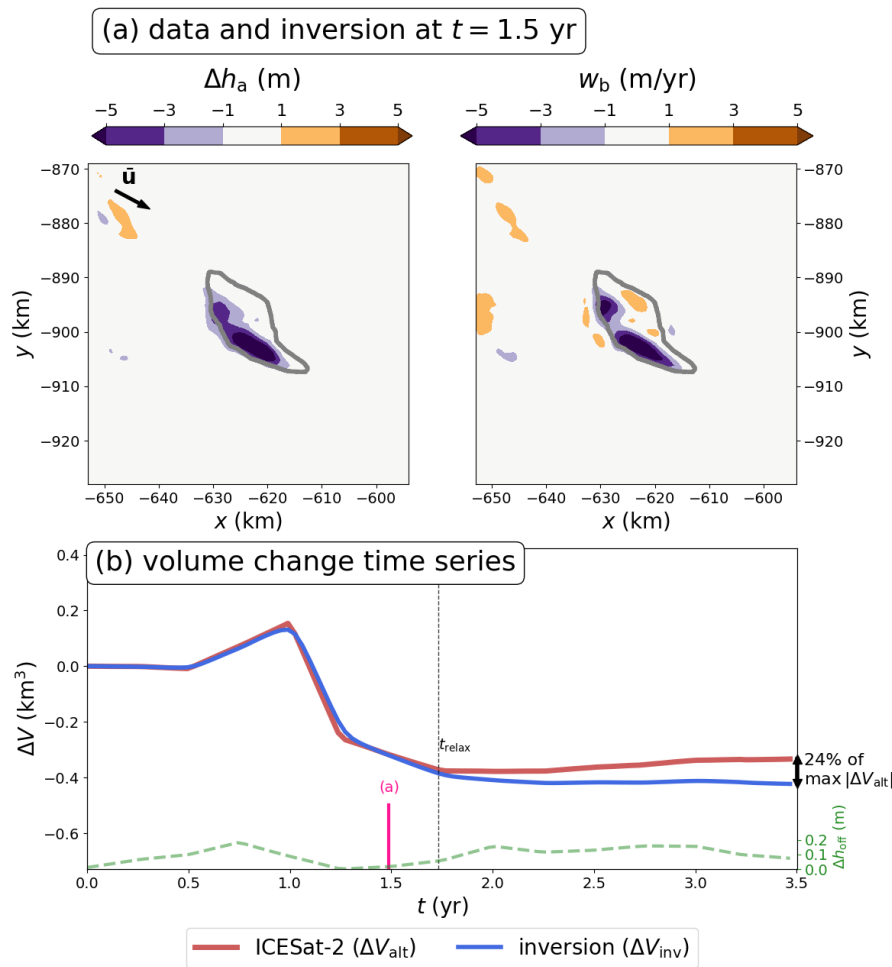


Fig. 5. Inversion results for subglacial lake Mac1. (a) Map-plane elevation anomaly and inversion at $t = 1.5$ yr. (b) Time series of the surface-derived volume change (ΔV_{alt}), the inversion-based volume change (ΔV_{inv}), and the off-lake component (Δh_{off}) that is removed prior to inversion. The gray contours in (a) and (b) show the boundaries used to compute the volume-change time series (Siegfried and Fricker, 2018). The ice flow direction is shown by the black arrow in (a). The maximum deviation between the surface-derived volume change and inversion is 0.09 km^3 , or 24% of the maximum amplitude of the surface-derived estimate. The parameters for this example are $\bar{H} = 926 \text{ m}$, $\bar{\eta} = 2.3 \times 10^{14} \text{ Pa s}$, $\bar{\beta} = 7.4 \times 10^{10} \text{ Pa s m}^{-1}$, $\bar{u} = 334 \text{ m yr}^{-1}$, and $\bar{v} = -178 \text{ m yr}^{-1}$. The viscous relaxation time associated with these parameters is $t_{\text{relax}} = 1.73 \text{ yr}$. The pink line marks the time step shown in (a). See Movie S4 for an animation of the inversion over all time steps.

260 latest subglacial boundary inventory (Siegfried and Fricker, 2018), which is a compilation of static active
261 subglacial lake outlines from a variety of sources that used mixed delineation methods.

262 ICESAT-2 EXAMPLES

263 Next, we will invert ICESat-2 data (ATL15 gridded elevation-change product) for the subglacial lakes
264 shown in Figure 1: Lake Mac1 beneath the MacAyeal Ice Stream (e.g., Fricker and others, 2010; Siegfried
265 and Fricker, 2018, 2021), Mercer Subglacial Lake at the confluence of Mercer Ice Stream and Whillans
266 Ice Stream (e.g., Fricker and others, 2007; Siegfried and Fricker, 2018, 2021; Siegfried and others, 2023),
267 Slessor₂₃ beneath Slessor Glacier (Siegfried and Fricker, 2018; Siegfried and others, 2021), Thw₁₇₀ beneath
268 Thwaites Glacier (Smith and others, 2017; Hoffman and others, 2020) and Byrd_{s10} beneath Byrd Glacier
269 in East Antarctica (Smith and others, 2009; Wright and others, 2014). These lakes have been the sub-
270 ject of numerous previous investigations and represent a wide range of filling-draining patterns, physical
271 conditions, and locations across the Antarctic Ice Sheet (Table 1). For these examples, it is important to
272 consider the reference time t_{ref} used to define the elevation anomaly in equation (23). We base our choices
273 on the lake activity leading up to the ICESat-2 epoch. For example, subglacial lake Mac1 showed little
274 activity since the beginning of the ICESat-2 epoch in 2018 (Siegfried and Fricker, 2021), suggesting that the
275 initial time in the ATL15 data is an appropriate choice of reference time. For Mac1, there is a maximum
276 discrepancy of $\sim 0.12 \text{ km}^3$ between the surface-based and inversion-based volume-change estimates, or 24%
277 of the maximum amplitude of the surface-derived estimate (Figure 5).

278 We also show inversions of Mercer Subglacial Lake (SLM), which displays multiple oscillations over the
279 ICESat-2 period (Figure 6). We set the reference time to be $t = 1.3 \text{ yr}$ after the initial time (i.e. around
280 the second peak in the time series), as this more closely corresponds to the long-term mean of Mercer
281 Subglacial Lake's oscillation pattern (Siegfried and Fricker, 2021). For this example, we find a maximum
282 discrepancy of $\sim 0.05 \text{ km}^3$ between the surface-based and inversion-based volume-change estimates, or 19%
283 of the maximum amplitude of the surface-derived estimate.

284 We also invert elevation anomalies from Slessor Glacier (lake Slessor₂₃) and Thwaites Glacier (lake
285 Thw₁₇₀). Slessor₂₃ shows a discrepancy of $\sim 0.52 \text{ km}^3$ between the volume-change estimates, which is
286 62% of the maximum amplitude of the surface-derived estimate (Figure 7). Thw₁₇₀ also shows a large
287 discrepancy of $\sim 0.21 \text{ km}^3$, or 49% of the maximum in the altimetry-based estimate (Figure 8). For
288 Slessor₂₃, the initial time in the ICESat-2 data appears to be close to the midpoint of a filling stage, so

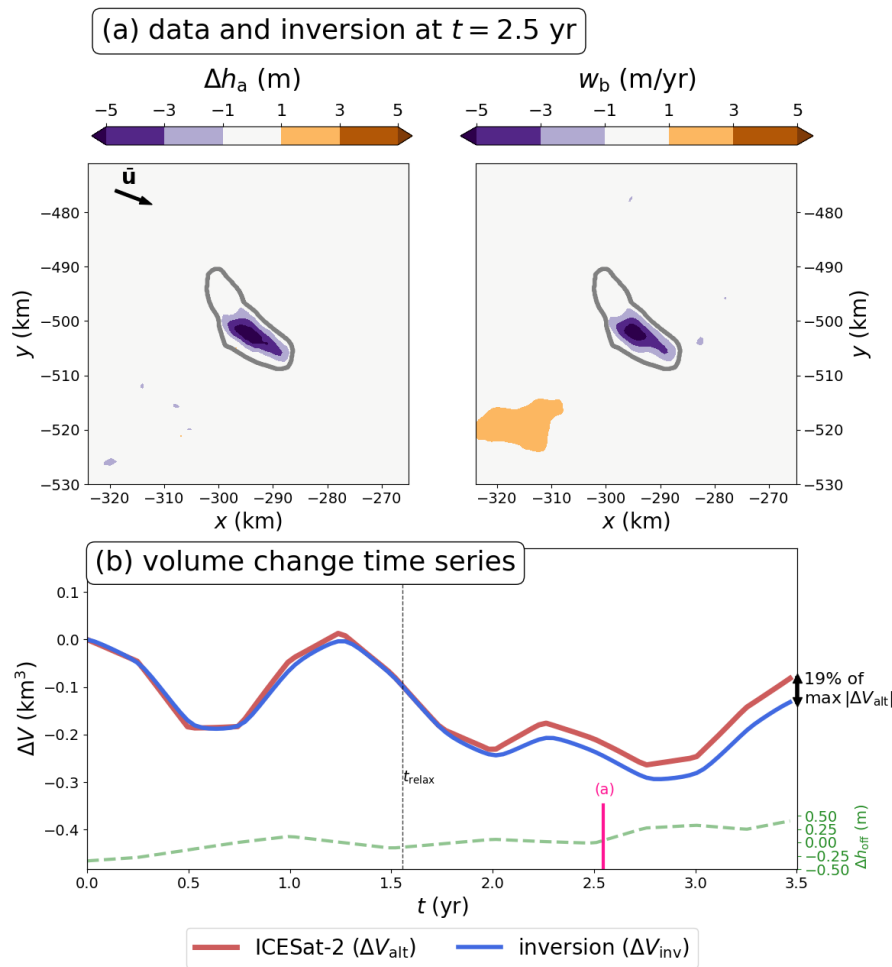


Fig. 6. Inversion results for Mercer Subglacial Lake (SLM in Figure 1). (a) Map-plane elevation anomaly and inversion at $t = 2.5$ yr. (b) Time series of the surface-derived volume change (ΔV_{alt}), the inversion-based volume change (ΔV_{inv}), and the off-lake component (Δh_{off}) that is removed prior to inversion. The gray contours in (a) and (b) show the boundaries used to compute the volume-change time series (Siegfried and Fricker, 2018). The ice flow direction is shown by the black arrow in (a). The maximum deviation between the surface-derived volume change and inversion in (b) is 0.05 km^3 , or 19% of the maximum amplitude of the surface-derived estimate. The parameters for this example are $\bar{H} = 1003 \text{ m}$, $\bar{\eta} = 2.2 \times 10^{14} \text{ Pa s}$, $\bar{\beta} = 3.7 \times 10^{11} \text{ Pa s m}^{-1}$, $\bar{u} = 172 \text{ m yr}^{-1}$, and $\bar{v} = -65 \text{ m yr}^{-1}$. The viscous relaxation time associated with these parameters is $t_{\text{relax}} = 1.56 \text{ yr}$. The pink line marks the time step shown in (a). See Movie S5 for an animation of the inversion over all time steps.

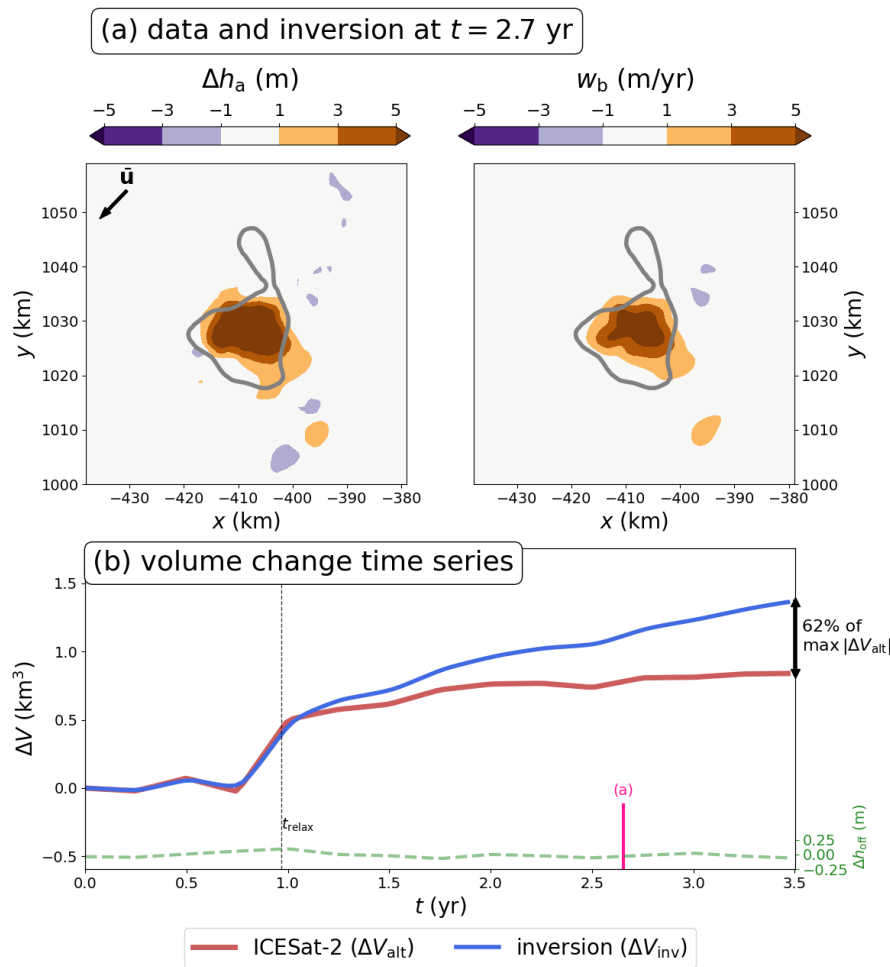


Fig. 7. Inversion results for subglacial lake Slessor₂₃. (a) Map-plane elevation anomaly and inversion at $t = 2.7$ yr. (b) Time series of the surface-derived volume change (ΔV_{ait}), the inversion-based volume change (ΔV_{inv}), and the off-lake component (Δh_{off}) that is removed prior to inversion. The gray contours in (a) and (b) show the boundaries used to compute the volume-change time series (Siegfried and Fricker, 2018). The ice flow direction is shown by the black arrow in (a). The maximum deviation between the altimetry-derived volume change and inversion in (b) is 0.52 km^3 , or 62% of the maximum amplitude of the surface-derived estimate. The parameters for this example are $\bar{H} = 1735 \text{ m}$, $\bar{\eta} = 2.4 \times 10^{14} \text{ Pa s}$, $\bar{\beta} = 2.7 \times 10^{10} \text{ Pa s m}^{-1}$, $\bar{u} = -141 \text{ m yr}^{-1}$, and $\bar{v} = -146 \text{ m yr}^{-1}$. The viscous relaxation time associated with these parameters is $t_{\text{relax}} = 0.97 \text{ yr}$. The pink line marks the time step shown in (a). See Movie S6 for an animation of the inversion over all time steps.

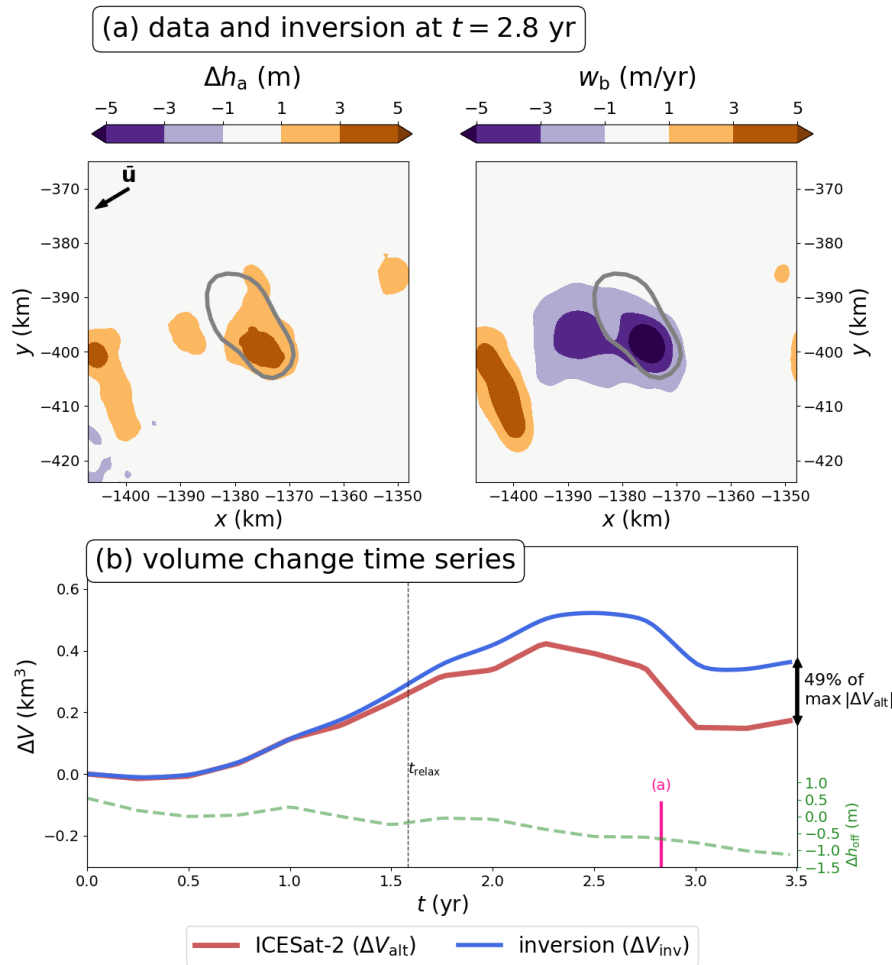


Fig. 8. Inversion results for subglacial lake Thw₁₇₀. (a) Map-plane elevation anomaly and inversion at $t = 2.8$ yr. (b) Time series of the surface-derived volume change (ΔV_{ait}), the inversion-based volume change (ΔV_{inv}), and the off-lake component (Δh_{off}) that is removed prior to inversion. The gray contours in (a) and (b) show the boundaries used to compute the volume-change time series (Smith and others, 2017). The ice flow direction is shown by the black arrow in (a). The maximum deviation between the altimetry-derived volume change and inversion is 0.21 km^3 , or 49% of the maximum amplitude of the surface-derived estimate. The parameters for this example are $\bar{H} = 2558$ m, $\bar{\eta} = 5.7 \times 10^{14}$ Pa s, $\bar{\beta} = 1.3 \times 10^{10}$ Pa s m^{-1} , $\bar{u} = -130$ m yr^{-1} , and $\bar{v} = -78$ m yr^{-1} . The viscous relaxation time associated with these parameters is $t_{\text{relax}} = 1.58$ yr. The pink line marks the time step shown in (a). See Movie S7 for an animation of the inversion over all time steps.

289 this reference time seems appropriate for defining the elevation anomaly (Siegfried and Fricker, 2018). On
290 the other hand, Thw_{170} appears to be coming out of a quiescent post-drainage period at the beginning of
291 the ICESat-2 period, so choosing the correct reference time is more ambiguous in this case (Hoffman and
292 others, 2020; Malczyk and others, 2020). For example, setting the reference time to $t = 1.5$ yr instead
293 results in a maximum discrepancy of ~ 0.075 km³ between the volume-change estimates for the Thw_{170}
294 inversion. This discrepancy arises because the magnitude of the elevation-change anomaly is diminished
295 when choosing the different reference time and less of the signal is attributed to the basal forcing. We
296 quantify the sensitivity to the reference time more thoroughly in Appendix A and highlight the main issues
297 in the discussion.

298 The common theme of the preceding examples is that they have ice viscosities on the order of $\bar{\eta} = 10^{14}$ Pa
299 s (Table 1) and volume-change discrepancies that are at least $\sim 20\%$ of the maximum of the altimetry-based
300 estimate (Figures 5-8). The range of basal drag coefficients and ice thicknesses across these examples (Table
301 1) suggests that the ice viscosity is the primary parameter controlling the volume-change discrepancies. At
302 higher viscosity values, the volume-change discrepancies diminish over the current ICESat-2 time period
303 because the viscous relaxation time exceeds the oscillation timescale. To illustrate this behaviour, we
304 inverted ICESat-2 data over subglacial lake Byrd_{s10} and found a much smaller discrepancy ($\sim 4\%$) between
305 the surface-based and inversion-based volume estimates (Figure 9). This lack of discrepancy arises because
306 the ice over this lake has a viscosity of $\bar{\eta} = 5 \times 10^{15}$ Pa s, an order of magnitude higher than the preceding
307 ICESat-2 examples. In this case, the surface and basal motion correspond more closely because the viscous
308 relaxation time, $t_{\text{relax}} = 13$ yr, is much longer than the current ICESat-2 time span. However, over decadal
309 timescales larger discrepancies are still possible for this parameter regime (e.g., Figure 3) unless the lake
310 oscillation period is small compared to the relaxation time (Stubblefield and others, 2021a).

311 DISCUSSION

312 Several practical and technical challenges are worth considering when applying the inverse method. From
313 a practical viewpoint, the primary challenge is deriving the elevation anomaly from the altimetry data. For
314 example, the inversion results may be sensitive to the details of how any regional thickening or thinning
315 trends are separated from the lake-related elevation changes (Fricker and Scambos, 2009; Smith and others,
316 2009; Siegfried and Fricker, 2018, 2021). The reference elevation profile that is used to define the elevation
317 anomaly from the data can also influence the inversion results, as we discussed in the case of subglacial lake

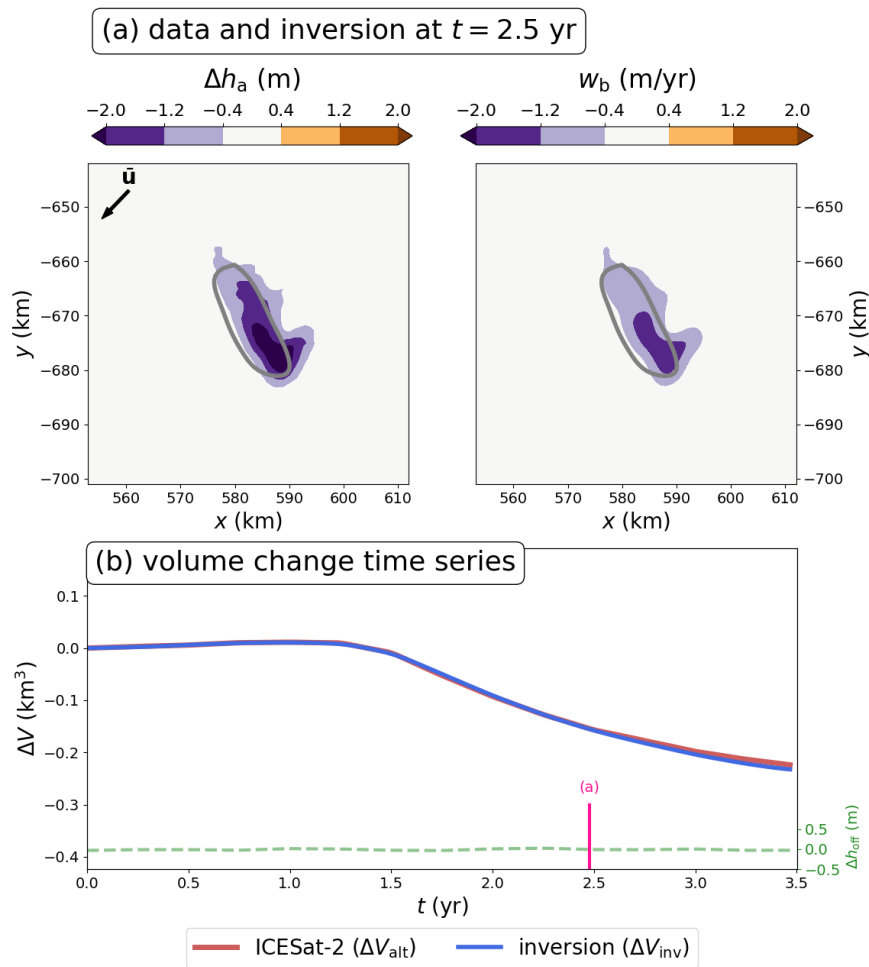


Fig. 9. Inversion results for subglacial lake Byrd_{s10}. (a) Map-plane elevation anomaly and inversion at $t = 2.5$ yr. (b) Time series of the surface-derived volume change (ΔV_{alt}), the inversion-based volume change (ΔV_{inv}), and the off-lake component (Δh_{off}) that is removed prior to inversion. The gray contours in (a) and (b) show the boundaries used to compute the volume-change time series. The ice flow direction is shown by the black arrow in (a). The maximum deviation between the altimetry-derived volume change and inversion is $9 \times 10^{-3} \text{ km}^3$, or 4% of the maximum amplitude of the surface-derived estimate. The parameters for this example are $\bar{H} = 2676 \text{ m}$, $\bar{\eta} = 5 \times 10^{15} \text{ Pa s}$, $\bar{\beta} = 1.4 \times 10^{11} \text{ Pa s m}^{-1}$, $\bar{u} = -9.4 \text{ m yr}^{-1}$, and $\bar{v} = -9.8 \text{ m yr}^{-1}$. The viscous relaxation time associated with these parameters is $t_{\text{relax}} = 13 \text{ yr}$. The pink line marks the time step shown in (a). See Movie S8 for an animation of the inversion over all time steps.

318 Thw₁₇₀. Likewise, choosing an appropriate reference elevation profile may be difficult when the ice-sheet
319 surface profile is heavily textured or the initial time in the data is during a volume-change event. In the
320 latter case, we have relied on records of lake oscillations from previous satellite altimetry missions to choose
321 appropriate reference times (Siegfried and Fricker, 2018, 2021). In Appendix A, we quantify the sensitivity
322 of inversion results to the choice of reference time for the synthetic data (Figure 10) and Thw₁₇₀ (Figure
323 11). The results highlight the importance of carefully considering the reference time or elevation profile
324 that is used to define the elevation-change anomaly (Appendix A). We leave further exploration of the
325 sensitivity of inversion results to preprocessing steps for future work.

326 The primary technical limitations of the perturbation-based inverse method is that the associated for-
327 ward models are inherently linear, posed on geometrically simple domains, and cannot deviate significantly
328 from the specified reference state. Although we have tested the validity of the method by inverting syn-
329 thetic data from a simple radially symmetric nonlinear problem (Figure 4), more complex problems could
330 require alternative methods. For example, we would caution against applying the method to complex stress
331 regimes like an ice-stream shear margin, which is the case for Engelhardt Subglacial Lake that lies beneath
332 the margin of the Whillans Ice Stream (Fricker and others, 2007; Siegfried and others, 2016). We have also
333 neglected any elastic components of ice deformation by assuming that ice flows as a viscous fluid because
334 the filling-draining events considered herein span multiple years. However, elastic deformation can arise
335 on shorter timescales near grounding lines when lake activity is related to tidal cycles (Milillo and others,
336 2017). Subglacial lakes have also been observed to drain on sub-weekly timescales during jökulhlaups in
337 Iceland (Björnsson, 2002; Evatt and Fowler, 2007). Moreover, we have assumed that all of the elevation
338 anomaly is driven by ice deformation rather than surface mass balance anomalies, which could arise, for
339 example, from snow infilling the lake depression (Malczyk and others, 2020).

340 We have also assumed that, to first order, the subglacial lakes do not coincide with reductions in
341 basal drag because the characteristic dipolar elevation anomaly associated with such slippery spots is
342 not discernible in the examples considered herein (e.g., Gudmundsson, 2003; Sergienko and others, 2007).
343 However, some large, inactive Antarctic subglacial lakes are known to coincide with slippery spots where
344 the ice surface is flat over most of the lake except on the upstream side where thinning occurs and the
345 downstream side where thickening occurs (Bell and others, 2006, 2007; Wright and Siegert, 2012). On the
346 other hand, several West Antarctic ice streams also have both subglacial lakes and localized regions of
347 anomalously high basal drag (sticky spots) in close proximity (Winberry and others, 2009; Sergienko and

348 Hulbe, 2011; Winberry and others, 2014; Siegfried and others, 2016). This coupling can arise when enhanced
349 basal traction provides a meltwater source for the lakes or when lake drainage causes channelisation that
350 removes water from surrounding regions of the bed (Sergienko and Hulbe, 2011). Joint inversion for basal
351 drag variations and lake activity would help to further refine our understanding of these coupled systems
352 and may be tractable if an additional data source like surface velocity is available.

353 In this study, we have focused primarily on estimating subglacial water-volume changes. Another appli-
354 cation of the inverse method will be estimating subglacial lake shorelines or areal extent. Lake boundaries
355 are currently defined using ice-surface deformation extent to generate static lake boundaries (Siegfried and
356 Fricker, 2018); however, these static boundaries were typically generated using lower spatial resolution
357 altimetry instruments than are available today. This static view of lake boundaries has resulted in a num-
358 ber of lake re-delineation attempts (e.g., Fricker and others, 2014; Siegfried and Fricker, 2018) and more
359 recent suggestions of time-variable lake boundaries (e.g., Neckel and others, 2021; Siegfried and Fricker,
360 2021). In our study, it is clear that static subglacial lake boundaries do not dependably encompass the
361 ICESat-2 surface height change observations (Figures 5-9) likely because lake shorelines vary temporally.
362 Additionally, recent numerical modeling shows the surface-derived boundaries can have a larger areal extent
363 than the true lake boundary at the base (Stubblefield and others, 2021a). With our inverse method, we
364 could attempt to reconstruct subglacial shoreline evolution by tracking the areal extent of the basal forcing
365 rather than the surface deformation. Improving the accuracy of subglacial-lake shoreline estimates in this
366 way could be valuable for site selection in future subglacial drilling projects (Tulaczyk and others, 2014;
367 Priscu and others, 2021) and thereby provide stronger constraints on subglacial microbial and geochemical
368 processes (Christner and others, 2014; Achberger and others, 2016; Davis and others, 2023).

369 The inverse method could be extended to estimate other subglacial hydrological quantities besides
370 water-volume changes. For example, the temporal derivative of the volume change can be related to the
371 relative volumetric water discharge into (or out of) the lake (Evatt and Fowler, 2007). The water discharge
372 naturally appears in models of glacial lakes that are coupled to subglacial channel evolution (Fowler, 1999,
373 2009; Kingslake, 2015; Carter and others, 2017; Stubblefield and others, 2019; Jenson and others, 2022).
374 Finally, an alternative to prescribing a basal vertical velocity anomaly would have been prescribing a
375 basal pressure anomaly. In particular, converting between vertical velocity and pressure perturbations is
376 straightforward with the spectral method employed here (e.g., Gudmundsson, 2003, equation 54). Pressure
377 perturbations could possibly be related to the subglacial effective pressure, the difference between the

378 cryostatic pressure and water pressure in the lake, since we have assumed that the pressure in the reference
379 state is cryostatic (cf. Evatt and Fowler, 2007; Stubblefield and others, 2021b). Estimating the effective
380 pressure or other hydrological quantities with altimetry would be valuable for further constraining the
381 physics of subglacial drainage systems.

382 CONCLUSIONS

383 We have introduced and applied an inverse method for estimating the basal forcing associated with sub-
384 glacial lake activity from ice-sheet altimetry. We have provided some validation of the small-perturbation
385 approach by inverting synthetic data from a nonlinear subglacial lake model to obtain a basal vertical
386 velocity field and water-volume change time series that agree with the nonlinear model. We then applied
387 the method to a collection of Antarctic subglacial lakes by inverting satellite altimetry data from NASA's
388 ICESat-2 mission. These results illustrate that there can be significant discrepancies between surface-based
389 estimation methods and the inversion due to the effects of viscous ice flow. In particular, the results show
390 that surface-based estimation methods can underestimate changes in subglacial water volume. The inverse
391 method provides a simple way to refine basal water budget contributions derived from active subglacial
392 lakes and further illuminate the physics of subglacial hydrological systems with satellite altimetry.

393 SUPPLEMENTARY MATERIAL

394 A link to the Supplementary material (Movies S1-S8 showing animations of Figures 3-9) will be placed
395 here.

396 DATA

397 All data used in this study are openly available:

- 398 ICESat-2 ATL15, Version 2 (<https://doi.org/10.5067/ATLAS/ATL15.002>),
399 WAVI ice-sheet model output (<https://doi.org/10.5285/5F0AC285-CCA3-4A0E-BCBC-D921734395AB>),
400 MEaSURES Phase-Based Antarctica Ice Velocity Map, Version 1 (<https://doi.org/10.5067/PZ3NJ5RXXRH10>),
401 MEaSURES BedMachine Antarctica, Version 3 (<https://doi.org/10.5067/FPSU0V1MWUB6>),
402 Subglacial lake inventory from Siegfried and Fricker (2018) (<https://doi.org/10.5281/zenodo.4914107>).
403 The code used to produce the results is openly available (<https://doi.org/10.5281/zenodo.8371416>).

404 **ACKNOWLEDGEMENTS**

405 A.G.S. thanks Jonathan Kingslake, Meredith Nettles, Ian Hewitt, and Brent Minchew for discussions
406 about the inverse problem. A.G.S. was supported by NSF (2012958). C.R.M. was supported by NSF
407 (2012958); ARO (78811EG); and NASA (80NSSC21M0329). M.R.S. and W.S. supported by NASA
408 (80NSSC21K0912).

409 **REFERENCES**

- 410 Achberger AM, Christner BC, Michaud AB, Priscu JC, Skidmore ML, Vick-Majors TJ, Adkins W, Anandakrishnan
411 S, Barbante C, Barcheck G, Beem L, Behar A, Beitch M, Bolsey R, Branecky C, Carter S, Christianson K, Edwards
412 R, Fisher A, Fricker H, Foley N, Guthrie B, Hodson T, Jacobel R, Kelley S, Mankoff K, McBryan E, Mikucki J,
413 Mitchell A, Powell R, Purcell A, Sampson D, Scherer R, Sherve J, Siegfried M and Tulaczyk S (2016) Microbial
414 community structure of subglacial Lake Whillans, West Antarctica. *Frontiers in Microbiology*, **7**(SEP), 1–13, ISSN
415 1664302X (doi: 10.3389/fmicb.2016.01457)
- 416 Arthern RJ, Hindmarsh RC and Williams CR (2015) Flow speed within the Antarctic ice sheet and its controls
417 inferred from satellite observations. *Journal of Geophysical Research: Earth Surface*, **120**(7), 1171–1188
- 418 Atkinson K and Han W (2009) *Theoretical numerical analysis*, volume 39. Springer, 3 edition
- 419 Balise MJ and Raymond CF (1985) Transfer of basal sliding variations to the surface of a linearly viscous glacier.
420 *Journal of Glaciology*, **31**(109), 308–318
- 421 Bell RE, Studinger M, Fahnestock MA and Shuman CA (2006) Tectonically controlled subglacial lakes on the flanks
422 of the Gamburtsev Subglacial Mountains, East Antarctica. *Geophysical Research Letters*, **33**(2)
- 423 Bell RE, Studinger M, Shuman CA, Fahnestock MA and Joughin I (2007) Large subglacial lakes in East Antarctica
424 at the onset of fast-flowing ice streams. *Nature*, **445**(7130), 904–907, ISSN 14764687 (doi: 10.1038/nature05554)
- 425 Björnsson H (2002) Subglacial lakes and jökulhlaups in iceland. *Global and Planetary Change*, **35**(3-4), 255–271
- 426 Bowling J, Livingstone S, Sole A and Chu W (2019) Distribution and dynamics of Greenland subglacial lakes. *Nature*
427 *communications*, **10**(1), 1–11
- 428 Budd W (1970) Ice flow over bedrock perturbations. *Journal of Glaciology*, **9**(55), 29–48
- 429 Carter SP, Fricker HA and Siegfried MR (2017) Antarctic subglacial lakes drain through sediment-floored canals: The-
430 ory and model testing on real and idealized domains. *Cryosphere*, **11**(1), 381–405, ISSN 19940424 (doi: 10.5194/tc-
431 11-381-2017)

- 432 Christner BC, Priscu JC, Achberger AM, Barbante C, Carter SP, Christianson K, Michaud AB, Mikucki JA,
433 Mitchell AC, Skidmore ML and others (2014) A microbial ecosystem beneath the West Antarctic ice sheet. *Nature*,
434 **512**(7514), 310–313
- 435 Cuffey KM and Paterson WSB (2010) *The physics of glaciers*. Academic Press
- 436 Davis CL, Venturelli RA, Michaud AB, Hawkings JR, Achberger AM, Vick-Majors TJ, Rosenheim BE, Dore JE,
437 Steigmeyer A, Skidmore ML and others (2023) Biogeochemical and historical drivers of microbial community
438 composition and structure in sediments from Mercer Subglacial Lake, West Antarctica. *ISME communications*,
439 **3**(1), 8
- 440 Evatt GW and Fowler AC (2007) Cauldron subsidence and subglacial floods. *Annals of Glaciology*, **45**, 163–168,
441 ISSN 02603055 (doi: 10.3189/172756407782282561)
- 442 Fowler A (1999) Breaking the seal at Grímsvötn, Iceland. *Journal of Glaciology*, **45**(151), 506–516
- 443 Fowler A (2009) Dynamics of subglacial floods. *Proceedings of the Royal Society A: Mathematical, Physical and*
444 *Engineering Sciences*, **465**(2106), 1809–1828
- 445 Fricker HA and Scambos T (2009) Connected subglacial lake activity on lower Mercer and Whillans Ice
446 Streams, West Antarctica, 2003–2008. *Journal of Glaciology*, **55**(190), 303–315, ISSN 00221430 (doi:
447 10.3189/002214309788608813)
- 448 Fricker HA, Scambos T, Bindschadler R and Padman L (2007) An active subglacial water system in West Antarctica
449 mapped from space. *Science*, **315**(5818), 1544–1548
- 450 Fricker HA, Scambos T, Carter S, Davis C, Haran T and Joughin I (2010) Synthesizing multiple remote-sensing
451 techniques for subglacial hydrologic mapping: application to a lake system beneath MacAyeal Ice Stream, West
452 Antarctica. *Journal of Glaciology*, **56**(196), 187–199
- 453 Fricker HA, Carter SP, Bell RE and Scambos T (2014) Active lakes of Recovery Ice Stream , East Antarc-
454 tica : a bedrock-controlled subglacial hydrological system. *Journal of Glaciology*, **60**(223), 1015–1030 (doi:
455 10.3189/2014JoG14J063)
- 456 Fricker HA, Siegfried MR, Carter SP and Scambos TA (2016) A decade of progress in observing and modeling
457 Antarctic subglacial water systems. *Philosophical Transactions of the Royal Society A: Mathematical, Physical*
458 *and Engineering Sciences*, **374**(2059), ISSN 1364503X (doi: 10.1098/rsta.2014.0294)
- 459 Glen JW (1955) The creep of polycrystalline ice. *Proceedings of the Royal Society of London. Series A. Mathematical*
460 *and Physical Sciences*, **228**(1175), 519–538

- 461 Goldberg D, Heimbach P, Joughin I and Smith B (2015) Committed retreat of smith, pope, and kohler glaciers over
462 the next 30 years inferred by transient model calibration. *The Cryosphere*, **9**(6), 2429–2446
- 463 Gray L, Joughin I, Tulaczyk S, Spikes VB, Bindschadler R and Jezek K (2005) Evidence for subglacial water transport
464 in the West Antarctic Ice Sheet through three-dimensional satellite radar interferometry. *Geophysical Research
465 Letters*, **32**(3), L03501, ISSN 0094-8276
- 466 Greve R and Blatter H (2009) *Dynamics of ice sheets and glaciers*. Springer Science & Business Media
- 467 Gudmundsson GH (2003) Transmission of basal variability to a glacier surface. *Journal of Geophysical Research:
468 Solid Earth*, **108**(B5)
- 469 Gudmundsson GH and Raymond M (2008) On the limit to resolution and information on basal properties obtainable
470 from surface data on ice streams. *The Cryosphere*, **2**(2), 167–178
- 471 Hanke M (2017) *A Taste of Inverse Problems: Basic Theory and Examples*. SIAM
- 472 Hoffman AO, Christianson K, Shapero D, Smith BE and Joughin I (2020) Brief communication: Heterogenous
473 thinning and subglacial lake activity on Thwaites Glacier, West Antarctica. *The Cryosphere*, **14**(12), 4603–4609
- 474 Hutter K, Legerer F and Spring U (1981) First-order stresses and deformations in glaciers and ice sheets. *Journal of
475 Glaciology*, **27**(96), 227–270
- 476 Jenson A, Amundson JM, Kingslake J and Hood E (2022) Long-period variability in ice-dammed glacier outburst
477 floods due to evolving catchment geometry. *The Cryosphere*, **16**(1), 333–347
- 478 Kingslake J (2015) Chaotic dynamics of a glaciohydraulic model. *Journal of Glaciology*, **61**(227), 493–502
- 479 Larour E, Utke J, Csatho B, Schenk A, Seroussi H, Morlighem M, Rignot E, Schlegel N and Khazendar A (2014)
480 Inferred basal friction and surface mass balance of the Northeast Greenland Ice Stream using data assimilation
481 of ICESat (Ice Cloud and land Elevation Satellite) surface altimetry and ISSM (Ice Sheet System Model). *The
482 Cryosphere*, **8**(6), 2335–2351
- 483 Le Brocq AM, Payne AJ and Vieli A (2010) An improved Antarctic dataset for high resolution numerical ice sheet
484 models (ALBMAP v1). *Earth System Science Data*, **2**(2), 247–260
- 485 Livingstone SJ, Sole AJ, Storrar RD, Harrison D, Ross N and Bowling J (2019) Brief communication: Subglacial
486 lake drainage beneath Isunguata Sermia, West Greenland: Geomorphic and ice dynamic effects. *The Cryosphere*,
487 **13**(10), 2789–2796

- 488 Livingstone SJ, Li Y, Rutishauser A, Sanderson RJ, Winter K, Mikucki JA, Björnsson H, Bowling JS, Chu W, Dow
489 CF and others (2022) Subglacial lakes and their changing role in a warming climate. *Nature Reviews Earth &
490 Environment*, **3**(2), 106–124
- 491 Malczyk G, Gourmelen N, Goldberg D, Wuite J and Nagler T (2020) Repeat subglacial lake drainage and filling
492 beneath Thwaites Glacier. *Geophysical Research Letters*, **47**(23), e2020GL089658
- 493 Markus T, Neumann T, Martino A, Abdalati W, Brunt K, Csatho B, Farrell S, Fricker H, Gardner A, Harding D
494 and others (2017) The Ice, Cloud, and land Elevation Satellite-2 (ICESat-2): science requirements, concept, and
495 implementation. *Remote sensing of environment*, **190**, 260–273
- 496 Milillo P, Rignot E, Mouginot J, Scheuchl B, Morlighem M, Li X and Salzer JT (2017) On the short-term grounding
497 zone dynamics of pine island glacier, west antarctica, observed with cosmo-skymed interferometric data. *Geophys-
498 ical Research Letters*, **44**(20), 10–436
- 499 Morlighem M (2022) Measures bedmachine antarctica, version 3 (doi: 10.5067/FPSU0V1MWUB6)
- 500 Morlighem M, Rignot E, Binder T, Blankenship D, Drews R, Eagles G, Eisen O, Ferraccioli F, Forsberg R, Fretwell
501 P and others (2020) Deep glacial troughs and stabilizing ridges unveiled beneath the margins of the Antarctic ice
502 sheet. *Nature Geoscience*, **13**(2), 132–137
- 503 Mosbeux C, Gillet-Chaulet F and Gagliardini O (2016) Comparison of adjoint and nudging methods to initialise ice
504 sheet model basal conditions. *Geoscientific Model Development*, **9**(7), 2549–2562
- 505 Mouginot J, Scheuchl B and Rignot E (2012) Mapping of ice motion in Antarctica using synthetic-aperture radar
506 data. *Remote Sensing*, **4**(9), 2753–2767
- 507 Mouginot J, Rignot E and B S (2019a) Measures phase-based antarctica ice velocity map, version 1 (doi:
508 10.5067/PZ3NJ5RXHR10)
- 509 Mouginot J, Rignot E and Scheuchl B (2019b) Continent-wide, interferometric SAR phase, mapping of Antarctic ice
510 velocity. *Geophysical Research Letters*, **46**(16), 9710–9718
- 511 Neckel N, Franke S, Helm V, Drews R and Jansen D (2021) Evidence of Cascading Subglacial Water Flow at
512 Jutulstraumen Glacier (Antarctica) Derived From Sentinel-1 and ICESat-2 Measurements. *Geophysical Research
513 Letters*, **48**(20), e2021GL094472
- 514 Priscu JC, Kalin J, Winans J, Campbell T, Siegfried MR, Skidmore M, Dore JE, Leventer A, Harwood DM, Duling
515 D and others (2021) Scientific access into Mercer Subglacial Lake: scientific objectives, drilling operations and
516 initial observations. *Annals of Glaciology*, **62**(85-86), 340–352

- 517 Rignot E, Mouginot J and Scheuchl B (2011) Ice flow of the Antarctic ice sheet. *Science*, **333**(6048), 1427–1430
- 518 Scambos TA, Berthier E and Shuman CA (2011) The triggering of subglacial lake drainage during rapid glacier
519 drawdown: Crane Glacier, Antarctic Peninsula. *Annals of Glaciology*, **52**(59), 74–82, ISSN 02603055 (doi:
520 10.3189/172756411799096204)
- 521 Sergienko O (2012) The effects of transverse bed topography variations in ice-flow models. *Journal of Geophysical*
522 *Research: Earth Surface*, **117**(F3)
- 523 Sergienko OV and Hulbe CL (2011) ‘Sticky spots’ and subglacial lakes under ice streams of the Siple Coast, Antarctica.
524 *Annals of Glaciology*, **52**(58), 18–22
- 525 Sergienko OV, MacAyeal DR and Bindschadler RA (2007) Causes of sudden, short-term changes in ice-stream surface
526 elevation. *Geophysical Research Letters*, **34**(22), 1–6, ISSN 00948276 (doi: 10.1029/2007GL031775)
- 527 Siegfried M and Fricker H (2021) Illuminating active subglacial lake processes with ICESat-2 laser altimetry. *Geo-*
528 *physical Research Letters*, **48**(14), e2020GL091089
- 529 Siegfried M, Venturelli R, Patterson M, Arnuk W, Campbell T, Gustafson C, Michaud A, Galton-Fenzi B, Hausner
530 M, Holzschuh S, Huber B, Mankoff K, Schroeder D, Summers P, Tyler S, Carter S, Fricker H, Harwood D, Leventer
531 A, Rosenheim B, Skidmore M, Priscu J and the SALSA Science Team (2023) The life and death of a subglacial
532 lake in West Antarctica. *Geology*, **51**(5), 434–438, ISSN 0091-7613 (doi: 10.1130/G50995.1)
- 533 Siegfried MR and Fricker HA (2018) Thirteen years of subglacial lake activity in Antarctica from multi-mission
534 satellite altimetry. *Annals of Glaciology*, **59**, 1–14, ISSN 0260-3055 (doi: 10.1017/aog.2017.36)
- 535 Siegfried MR, Fricker HA, Carter SP and Tulaczyk S (2016) Episodic ice velocity fluctuations triggered by
536 a subglacial flood in West Antarctica. *Geophysical Research Letters*, **43**(6), 2640–2648, ISSN 19448007 (doi:
537 10.1002/2016GL067758)
- 538 Siegfried MR, Schroeder DM, Sauthoff W and Smith B (2021) Investigating a large subglacial lake drainage in east
539 antarctica with ice-penetrating radar. In *SEG/AAPG/SEPM First International Meeting for Applied Geoscience*
540 *& Energy*, OnePetro
- 541 Smith B, Sutterley T, Dickinson S, Jelley B, Felikson D, Neumann TA, Fricker H, Gardner A, Padman L, Markus
542 T, Kurtz N, Bhardwaj S, Hancock D and Lee J (2022) ATLAS/ICESat-2 L3B Gridded Antarctic and Arctic Land
543 Ice Height Change, Version 2 (doi: 10.5067/ATLAS/ATL15.002)
- 544 Smith BE, Fricker HA, Joughin IR and Tulaczyk S (2009) An inventory of active subglacial lakes in Antarctica
545 detected by ICESat (2003–2008). *Journal of Glaciology*, **55**(192), 573–595

- 546 Smith BE, Gourmelen N, Huth A and Joughin I (2017) Connected subglacial lake drainage beneath Thwaites Glacier,
547 West Antarctica. *Cryosphere*, **11**(1), 451–467, ISSN 19940424 (doi: 10.5194/tc-11-451-2017)
- 548 Stadler G (2009) Elliptic optimal control problems with L1-control cost and applications for the placement of control
549 devices. *Computational Optimization and Applications*, **44**(2), 159
- 550 Stearns LA, Smith BE and Hamilton GS (2008) Increased flow speed on a large east antarctic outlet glacier caused
551 by subglacial floods. *Nature Geoscience*, **1**(12), 827–831, ISSN 17520894 (doi: 10.1038/ngeo356)
- 552 Stubblefield AG (2022) *Modelling the dynamics and surface expressions of subglacial water flow*. Ph.D. thesis,
553 Columbia University
- 554 Stubblefield AG, Creyts TT, Kingslake J and Spiegelman M (2019) Modeling oscillations in connected glacial lakes.
555 *Journal of Glaciology*, **65**(253), 745–758
- 556 Stubblefield AG, Creyts TT, Kingslake J, Siegfried MR and Spiegelman M (2021a) Surface Expression and Apparent
557 Timing of Subglacial Lake Oscillations Controlled by Viscous Ice Flow. *Geophysical Research Letters*, **48**(17),
558 e2021GL094658 (doi: <https://doi.org/10.1029/2021GL094658>), e2021GL094658 2021GL094658
- 559 Stubblefield AG, Spiegelman M and Creyts TT (2021b) Variational formulation of marine ice-sheet and subglacial-
560 lake grounding-line dynamics. *Journal of Fluid Mechanics*, **919**, A23 (doi: 10.1017/jfm.2021.394)
- 561 Thorsteinsson T, Raymond CF, Gudmundsson GH, Bindschadler RA, Vornberger P and Joughin I (2003) Bed
562 topography and lubrication inferred from surface measurements on fast-flowing ice streams. *Journal of Glaciology*,
563 **49**(167), 481–490
- 564 Tulaczyk S, Mikucki JA, Siegfried MR, Priscu JC, Barcheck CG, Beem LH, Behar A, Burnett J, Christner BC, Fisher
565 AT, Fricker HA, Mankoff KD, Powell RD, Rack F, Sampson D, Scherer RP and Schwartz SY (2014) WISSARD
566 at Subglacial Lake Whillans, West Antarctica: Scientific operations and initial observations. *Annals of Glaciology*,
567 **55**(65), 51–58, ISSN 02603055 (doi: 10.3189/2014AoG65A009)
- 568 Turcotte DL and Schubert G (2002) *Geodynamics*. Cambridge university press
- 569 Virtanen P, Gommers R, Oliphant TE, Haberland M, Reddy T, Cournapeau D, Burovski E, Peterson P, Weckesser
570 W, Bright J, van der Walt SJ, Brett M, Wilson J, Millman KJ, Mayorov N, Nelson ARJ, Jones E, Kern R,
571 Larson E, Carey CJ, Polat İ, Feng Y, Moore EW, VanderPlas J, Laxalde D, Perktold J, Cimrman R, Henriksen
572 I, Quintero EA, Harris CR, Archibald AM, Ribeiro AH, Pedregosa F, van Mulbregt P and SciPy 10 Contributors
573 (2020) SciPy 1.0: Fundamental Algorithms for Scientific Computing in Python. *Nature Methods*, **17**, 261–272 (doi:
574 10.1038/s41592-019-0686-2)

- 575 Vogel CR (2002) *Computational Methods for Inverse Problems*. Society for Industrial and Applied Mathematics (doi:
576 10.1137/1.9780898717570)
- 577 Weertman J (1957) On the sliding of glaciers. *Journal of glaciology*, **3**(21), 33–38
- 578 Winberry JP, Anandakrishnan S and Alley RB (2009) Seismic observations of transient subglacial water-flow beneath
579 MacAyeal Ice Stream, West Antarctica. *Geophysical Research Letters*, **36**(11)
- 580 Winberry JP, Anandakrishnan S, Alley RB, Wiens DA and Pratt MJ (2014) Tidal pacing, skipped slips and the
581 slowdown of Whillans Ice Stream, Antarctica. *Journal of Glaciology*, **60**(222), 795–807
- 582 Wingham DJ, Siegert MJ, Shepherd A and Muir AS (2006) Rapid discharge connects Antarctic subglacial lakes.
583 *Nature*, **440**(7087), 1033–1036, ISSN 14764687 (doi: 10.1038/nature04660)
- 584 Wright A and Siegert M (2012) A fourth inventory of Antarctic subglacial lakes. *Antarctic Science*, **24**(6), 659–664,
585 ISSN 09541020 (doi: 10.1017/S095410201200048X)
- 586 Wright A, Young D, Bamber J, Dowdeswell J, Payne A, Blankenship D and Siegert M (2014) Subglacial hydrological
587 connectivity within the Byrd Glacier catchment, East Antarctica. *Journal of Glaciology*, **60**(220), 345–352

588 APPENDIX A - SENSITIVITY TO REFERENCE TIME

589 As noted in the results and discussion, the primary challenge of applying the inverse method in practice is
590 defining the elevation-change anomaly from the data. We must choose a reference time t_{ref} to define the
591 anomaly through equation (23). To explore this sensitivity further, we inverted the synthetic data (Figure
592 3) after re-defining the anomaly to be zero at a range of incorrect reference times. The results show that
593 choosing an appropriate reference time has a strong influence on the validity of the inversion. Choosing
594 an incorrect reference time can cause significant deviations between the inversion and the true solution
595 (Figure 10).

596 We repeated the experiment by inverting the Thw₁₇₀ data after re-defining the anomaly to be zero at
597 a range of alternative reference times (Figure 11). We find that none of the options correspond exactly to
598 the altimetry-based estimate over the ICESat-2 time period, although the earlier reference times ($t_{\text{ref}} \leq 1$)
599 correspond more closely to the expected behavior of a lake undergoing a filling stage (e.g., Figure 3). Even
600 so, it not entirely clear based on previously published data which option is the most valid (Hoffman and
601 others, 2020). Further investigation to determine when local perturbations in glacier surface elevation reach
602 a viscously relaxed state in more complex settings (e.g., Thwaites Glacier) would be valuable.

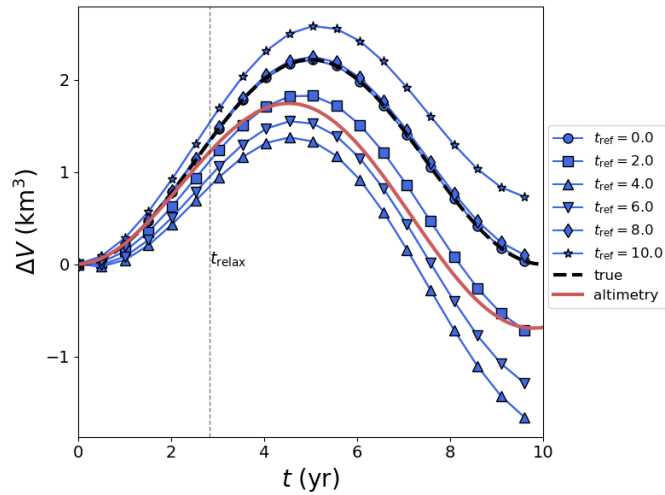


Fig. 10. Inversion of synthetic data from Figure 3 after redefining the reference time t_{ref} in equation (23) to a range of incorrect values. The correct reference time in this example is $t_{\text{ref}} = 0$. Significant deviations between the inversion and true solution can occur if an incorrect reference time is chosen.

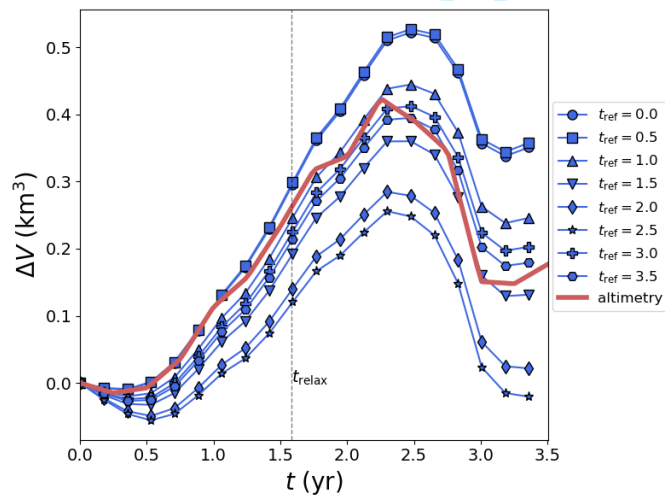


Fig. 11. Inversion of the Thw_{170} data from Figure 8 after redefining the reference time t_{ref} in equation (23) to a range of alternative values.